

Mechanical and Frictional Properties of Nanoparticle Monolayers Grafted on Functionalized Mica Substrates

Xavier Banquy,[†] X. X. Zhu,[‡] and Suzanne Giasson^{*,†,‡}

Faculty of Pharmacy, and Department of Chemistry, Université de Montréal, C.P. 6128, succursale Centre-ville, Montréal, Québec, Canada H3C 3J7

Received: April 24, 2008; Revised Manuscript Received: June 13, 2008

Normal and lateral forces between two opposing monolayers of grafted polymer nanoparticles (NPs) were measured using the Surface Forces Apparatus in a humid atmosphere. The NPs made of *N,N*-diethylacrylamide and 2-hydroxyethyl methacrylate have a hydrodynamic diameter of ca. 660 nm at 25 °C. The effect of surface roughness was studied by creating surface asperities using different NP grafting densities ranging from 0.41 to 2.63 NPs/ μm^2 . An increase in the NPs grafting density gave rise to an increase in surface roughness and to a deformation of the nanoparticles caused by the lateral pressure between neighboring particles. An elastoplastic behavior of the nanoparticles was observed for large grafting densities, while a purely elastic behavior was observed for small grafting densities. The lateral forces measured between two opposing NP monolayers sliding past each other followed Amontons' law for all grafting densities. The friction coefficient between the surfaces appeared to increase significantly with an increase in surface roughness, which was inherent to an increase in the elastoplastic behavior of the NP monolayers.

Introduction

The development of techniques for measuring surface forces such as the surface forces apparatus (SFA) and the atomic force microscope (AFM) allowed the fundamental understanding of tribological and adhesive behavior of materials to be significantly improved.^{1–4} The friction coefficient, defined as the tangential force required to maintain the sliding between two surfaces divided by the normal force between them, depends on several parameters, such as material mechanical and chemical properties, the surface roughness, and the relative sliding velocity of the surfaces.⁵ The mechanical properties and the roughness of the surfaces were first taken into account in the contact mechanics theory developed by Greenwood and Williamson (GW).⁶ Their model, which has been widely used, considers that all asperities have the same geometry, that they are in a nonadhesive Hertzian contact, and that there is an exponential distribution of summit heights. GW's model predicts a linear dependence between the real contact area and the applied load as described by Amontons' law. On the basis of GW's approach, more elaborated theoretical models have been proposed for non-Gaussian distribution of summit heights and for self-affine surfaces.⁷ A recent study has focused on the role of the surface roughness in the frictional behavior of a purely elastic polymer surface in adhesive contact with a smooth mica surface.⁸ This study shows that the adhesion-controlled friction, or static friction, decreases as the surface roughness increases, which is consistent with a decrease in the real contact area. However, no clear relationship between the kinetic or sliding friction and roughness could be evidenced. Experimental evidence of a reliable relationship between surface roughness and mechanical and frictional properties remains a challenging task because of the difficulty in building model systems with well-controlled mechanical and physical properties.

In the present article, we investigated the relationship between surface roughness and kinetic friction using polymeric nanoparticles (NPs) to create elastoplastic asperities. The NPs were grafted on a hard smooth functionalized mica surface. Surface roughness was varied by using different NP surface coverage or grafting densities. The interaction forces, the contact mechanics, and the frictional properties of two opposing identical NP-coated surfaces in air at a 30% relative humidity (RH) were studied using the surface forces apparatus.

Materials and Methods

General Details. Ruby mica sheets were purchased from S & J Trading Inc. (Glen Oaks, NY, USA). Plasma Prep II from SPI Supplies was used to activate mica surfaces using argon (5.0 grade) and MilliQ quality water. Milli-Q quality water was obtained from a Millipore Gradient A 10 purification system (resistance 18.2 M Ω .cm, TOC = 4 ppb). Anhydrous ethylene glycol 99.98% (EG), aminopropyltriethoxy silane (APTES), glutaraldehyde (25% w/w in water), potassium persulfate (KPS), and sodium cyanoborohydride (NaBH₃CN, 5 M in 1 M NaOH aqueous solution) were purchased from Aldrich.

Nanoparticle Synthesis. NPs were synthesized as previously reported.⁹ The monomers (diethylacrylamide (DEA) 90% mol and 2-hydroxyethyl methacrylate (HEMA) 10% mol, total amount of 26.5 mM in water), bisacrylamide (1.5% mol), and sodium dodecylsulfate (0.040 g) were added to 200 mL of Milli-Q water under stirring followed by nitrogen purging for 30 min at 70 °C. KPS (0.120 g) dissolved in 15 mL of Milli-Q water was subsequently added to the solution. The reaction was allowed to proceed for 4 h, and then the milky suspension was cooled at room temperature before filtering through 2.0 μm Millipore Isopore membrane filters. The filtrate was centrifuged for 40 min at about 15,000 rpm. The polymer nanoparticles were collected and purified by dialysis for 1 week in Milli-Q water. The diameter of the NPs synthesized using this protocol is 660 \pm 25 nm in water at 25 °C as measured by dynamic light scattering.⁹

* To whom correspondence should be addressed. E-mail: suzanne.giasson@umontreal.ca.

[†] Faculty of Pharmacy.

[‡] Department of Chemistry.

Atomic Force Microscopy (AFM). AFM imaging was carried out using a Multimode Dimension 3100 AFM and a NanoScope IIIa controller (Digital Instruments) operated in tapping mode. Aluminum coated silicon tips from NanoWorld (ARROW-NCR-20, force constant of 42 N/m, resonance frequency between 270 and 290 kHz) were used for all scanned samples. Data analysis was performed using the NanoScope III software (version 5.30r3). In order to measure the surface coverage and the pair correlation function of the grafted NPs, 10 images (30×30 nm) were captured on the surfaces after the SFA experiments. All images were taken at 25 °C in air at 30% RH.

XPS Characterization. XPS analysis of the surfaces was performed using Kratos Ultra (Kratos Analytical, UK) at an incidence angle of 70°. The pressure in the analysis chamber was maintained at 10^{-9} Torr. The electron source was an Al monochromator ($h\nu = 1486.6$ eV) with a power of $15 \text{ kV} \times 15 \text{ mA}$. The experimental spectral resolution was evaluated to be 0.5 eV. Energy calibration was carried out by placing the hydrocarbon peak in the C 1s spectrum at 285.0 eV. Single survey scan spectra (0–1000 eV) were recorded for each sample with a pass energy of 80 eV and steps of 1.0 eV. The analyzed surface area was $700 \mu\text{m} \times 300 \mu\text{m}$. Charge neutralization was achieved with an electron flood gun.

Reactive Layer Preparation. All surface manipulations were performed in a clean laminar airflow cabinet in order to prevent dust deposition on the surfaces. All glassware was carefully cleaned in a bath of KOH saturated isopropyl alcohol followed by an intensive rinsing with MilliQ water.

Grafting of APTES was performed on plasma activated mica surfaces using a modified protocol of the chemical evaporation technique^{10,11} as previously reported.^{12,13} Plasma treatment was used to generate silanol groups on the mica surfaces. Mica surfaces were placed in a plasma chamber under a vacuum pressure of 0.5 mTorr. Argon and water vapor were then introduced at partial pressures of 80 mTorr and 300 mTorr, respectively. Plasma activation was performed for 5 min at 40 W. After the activation, the mica surfaces were left under vacuum (0.5 mTorr) for 5 min. Then, the mica surfaces were transferred into an evaporation chamber and stored under vacuum (1.6 mmHg). The evaporation chamber was connected via a valve to a small glass reservoir containing 100 μL of APTES. After purging the evaporation chamber for 15 min, the valve was opened allowing APTES vapor to react with activated mica surfaces. During this step, vacuum was maintained in order to ensure a constant flux of APTES vapor in the chamber and to avoid condensation of APTES on the activated mica surfaces. Evaporation was allowed to proceed for 4 h. The valve was closed, and remnant APTES vapor was pumped out for 2 h. The APTES covalent grafting was completed by annealing the surfaces for 30 min at 120 °C under atmospheric pressure. Then, the surfaces bearing grafted APTES molecules were immersed in a 1% (w/w) water solution of glutaraldehyde overnight, where the coupling reaction between APTES amine function and glutaraldehyde carbonyl function took place in the presence of NaBH_3CN as previously reported.^{14,15} The resulting glutaraldehyde functionalized mica surfaces (Glu-surfaces) were thoroughly rinsed with Milli-Q water prior to nanoparticle deposition.

Nanoparticles Deposition. The deposition was performed using the horizontal convective evaporation method.¹⁶ Glass coverslips were cleaned in a piranha solution ($\text{H}_2\text{O}_2/\text{H}_2\text{SO}_4$, 30/70, v/v) at 40 °C during 10 min and thoroughly rinsed with Milli-Q water. A clean glass coverslip applicator was placed over a Glu-surface at an angle of 15°. The separation distance

between the applicator and the Glu-surface during the deposition process was kept constant between 50 and 100 μm . Prior to translation of the Glu-surface, a drop (25 μL) of NP suspension was placed between the applicator and the surface. As the Glu-surface was translated at a fixed velocity, the NP suspension drop could spread on the substrate, forming a uniform thin film of nanoparticles. The grafting of the NPs on Glu-surfaces occurred through the reaction between the pendant aldehyde functions on Glu-surfaces and the ethoxy groups of the NPs. The deposition process was carried out on a vibration isolated table in a closed sealed box at constant temperature (25 °C) and relative ambient humidity ($30 \pm 3\%$ RH).

Surface Forces Measurements. Normal Interactions. Measurements of normal interaction forces F_N between two opposing NP-coated surfaces as a function of separation distance were carried out using a surface forces apparatus (SFA 2000) whose principle is described in detail elsewhere.^{17,18} The interaction force is measured by the deflection of a spring cantilever (spring constant of 1000 N/m) that supports the lower surface. The distance between the surfaces is determined using the Fringes of Equal Chromatic Order.¹⁷ Back-silvered mica surfaces were glued silver side down on the SFA cylindrical disks (curvature radius of 2 cm) using an optical adhesive (Norland 81 UV cured glue, UK). The two disks were mounted in the SFA chamber in a cross cylinder geometry and brought into mica adhesive contact in humid air in order to determine a reference position (mica–mica contact) using the FECO fringes. Afterward, the cylindrical disks were dismounted from the SFA chamber for the mica functionalization (Glu-surface). The Glu-surfaces were mounted back in the SFA chamber at the same position as the initial one in order to measure the thickness of the reactive layer. The reference distance ($D = 0$) reported in the force profiles was set as the adhesive contact, under no external applied load, between the two Glu-surfaces in air. The disks were dismounted one more time for carrying the NP deposition, then the surfaces were mounted in the SFA chamber (at the same previous position), and the whole system was equilibrated for 8 h at 25 °C and ambient relative humidity (30% RH).

The configuration of the system is illustrated in Figure 1 and consists of two opposing mica surfaces bearing grafted NPs with the same grafting density. The normal interaction forces F_N between the two NP-coated surfaces as a function of surface separation were determined on approaching (compression) and separating (decompression) the surfaces step by step as previously described.¹⁹

The surfaces were allowed to equilibrate for ca. 2 min between each change in separation distance prior to the force measurement. The approaching and separating velocities of the lower surface were 0.2 nm/s. Experiments were reproduced twice with two different pairs of mica surfaces. Force profiles and friction measurements were performed on an average of three contact positions on each pair of surfaces during a period of 3 days. The illustrated curves represent the average force profiles with a standard deviation in measuring forces of ca. 0.1 mN/m.

Friction Measurement. The friction force F_S was measured by displacing the upper surface horizontally using a motor-driven sliding device as described elsewhere.²⁰ The sliding velocity was computer-controlled and measured before each experiment using a laser displacement detection device (Keyence LKG10 laser head, Canada). The upper surface was connected to a vertical cantilever spring, whose lateral deflection, allowing friction force to be determined, was measured using strain gauges.²⁰ The detection limit of the friction force was 3×10^{-3}

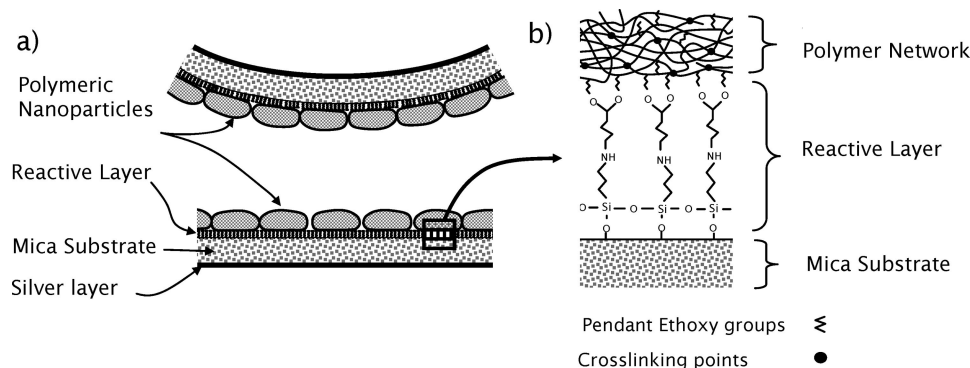


Figure 1. (a) Schematic of the configuration used for the SFA experiments. (b) Chemical attachment of the polymeric nanoparticles to mica substrate.

mN, and the signal noise rms was 1×10^{-3} mN. Using this device, the lateral sliding speed could be varied from 0.2 to 3.0 $\mu\text{m}\cdot\text{s}^{-1}$. Before measuring the friction forces, three cycles of normal compression/decompression were performed on the same contact position. The surfaces were compelled to slide past each other three times on the same sliding path back and forth. All friction measurements were made over a traveled distance sufficient to reach steady-state sliding, i.e., when the friction force to maintain smooth sliding is constant.

Results

Characterization of Glu-Surfaces and NP monolayers.

Chemical evidence of the presence of APTES on activated mica surfaces was obtained by XPS analysis. Single scans on the APTES treated mica substrates revealed the presence of a N1s peak at 399.19 eV, which was not detected on nontreated mica surfaces (see Figure 2a and b). High resolution scans allowed the molecular conformation of the grafted APTES molecules to be assessed. As seen in Figure 2c, the N1s peak presents a shoulder toward high binding energies, which is characteristic of the presence of nitrogen protonation and hydrogen bonding.²¹ The amount of nonprotonated molecules estimated via the area under the corresponding peaks corresponds to ca. 71% of the grafted APTES. These nonprotonated species are known to be oriented up toward the surface.²¹ Our results are in good agreement with reported studies on APTES grafting from solution on activated mica and silica surfaces.^{22–24}

The presence of APTES on the mica surfaces was also evidenced by simultaneously measuring the thickness and the refractive index of the grafted APTES layer in air at 25 °C using the SFA. The measured layer thickness (1.2 ± 0.4 nm) and the refractive index (1.43 ± 0.03) are in good agreement with values previously reported for the APTES monolayer on silicon wafers.²¹ The total thickness resulting from glutaraldehyde grafting was 2.7 ± 0.7 nm. AFM imaging of the APTES functionalized mica and Glu-surfaces revealed very smooth surfaces with subnanometric roughness (rms of 0.478 and 0.625, nm respectively).

In order to evaluate the stability of the NP anchorage, the variation of the NP surface coverage on the Glu-surfaces immersed in water was measured as a function of time using AFM. The results (Figure 3) show that the NPs deposited on the Glu-surfaces were stable over 72 h of immersion in water compared to the NPs deposited on bare mica surfaces, which desorbed instantaneously.

Several parameters are known to influence the surface coverage of NP monolayers deposited using the horizontal evaporation technique.²⁵ The translating velocity of the substrate

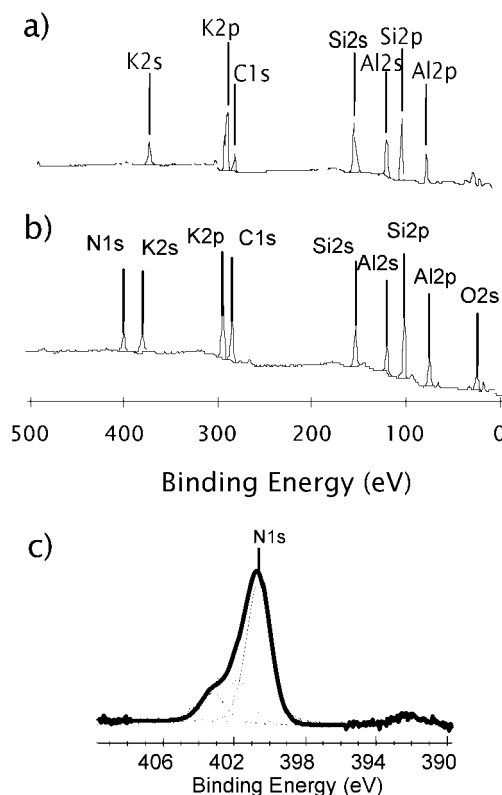


Figure 2. XPS analysis of (a) an activated mica surface and of (b) an APTES monolayer grafted on an activated mica surface. (c) XPS core-level N1s spectrum of APTES grafted on an activated mica surface.

and the nanoparticle suspension concentration have shown to control the final areal density.^{16,26} As shown in Figure 4, the NP grafting density decreases exponentially with a decrease in NP concentration or with an increase in the translating velocity. Similar results were observed for hard spheres deposited on glass substrates.^{16,25–27}

Spatial distribution of the NPs on Glu-surfaces was assessed by measuring the radial pair correlation function (RPCF). Figure 5 illustrates the AFM images of the NP monolayers with the measured RPCF for three different NP surface densities. The spatial distribution of the NPs within the monolayers does not display any long-range order (Figure 5a). A strong decay of the correlation peaks within a few NP radius up to an average value of 1 is observed for the three NP monolayers. The position of the first correlation peak, i.e., the average distance between the closest neighbors, decreases with an increase in NP surface density. As a reference, the NP assembly forms a long-range ordered two-dimensional (2D) crystal array on a bare mica

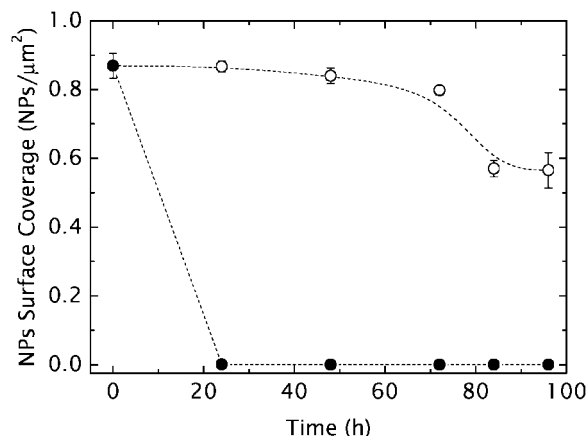


Figure 3. Variation of the nanoparticle surface coverage as a function of immersion time in water on ●, activated mica surface and ○, Glu-surfaces. The dashed lines are a guide for the eye.

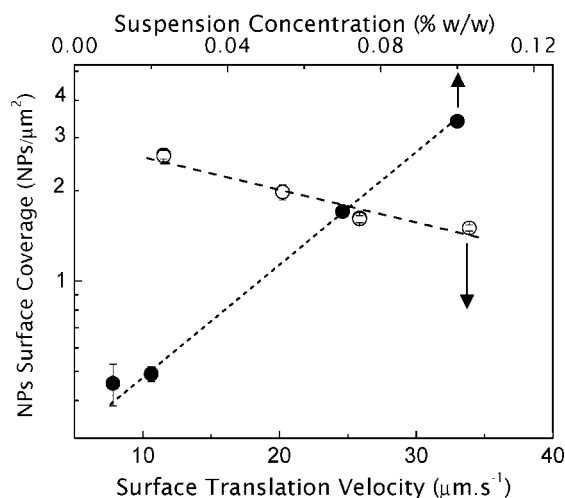


Figure 4. Variation of the nanoparticle surface coverage with the substrate translating velocity and the suspension concentration. Data were obtained using AFM in air at 25 °C and 30% RH.

surface (Figure 5c). The lack of a long-range NP order on Glu-surfaces arises from the reduced mobility of the NPs in comparison with that of the bare mica substrate. On bare mica, the NPs can move easily while the solvent is evaporating, allowing the 2D array to be formed by self-assembly. Because of water evaporation and capillary forces between the adjacent particles, the mobile particles form a crystal array. This process is not expected to occur on adhering substrates such as Glu-surfaces because the covalent bonds between the NPs and the surface limit their mobility and therefore their ordering during water evaporation.

The NPs can undergo large deformations during solvent evaporation, which can drastically change the surface topography of the monolayer and its roughness. The NPs were assumed to reach their equilibrium conformation after 8 h of storage at 25 °C in 30% RH atmosphere, as no variations in NPs height and size were measured using SFA (data not shown). For low surface coverage, isolated NPs on Glu-surfaces exhibit an oblate shape with 700 nm in diameter and 28 nm in thickness as measured by AFM (data not shown). As reference, the hydrodynamic diameter of these NPs in water is approximately 660 nm at 25 °C.⁹ Surface roughness of the NP coated surfaces was characterized by the rms (R_q) and rms slope (R_{dq}) measured by AFM. Results reported in Table 1 show an increase in R_{dq} and R_q (R_q varying from 5.5 to 10.6 nm) with an increase in the NP grafting density (from 0.41 NPs/ μm^2 and 2.63 NPs/ μm^2).

Normal Forces between NP Monolayers. The normal interaction forces between two identical NP monolayers were performed for four different NP grafting densities (0.41, 1.70, 1.97, and 2.63 NPs/ μm^2) under 30% RH conditions at 25 °C. The results are illustrated in Figure 6. The force profiles obtained at 1.97 and 2.63 NPs/ μm^2 were very similar, and therefore, only the profiles at 2.63 NPs/ μm^2 are presented for clarity. For large NP grafting densities (1.97 and 2.63 NPs/ μm^2), the first compression force profile shows an s-shape typical of the behavior of brush-like polymers in good solvents.²⁸ This typical s-shape in the interaction profile arises from the balance between the excluded volume repulsion that tends to stretch the polymers and the entropic polymer elasticity that tends to decrease polymer size. The onset of the interaction forces upon compression, arbitrarily set to the separation distance at which the normalized interaction force ($F_N/2\pi R$) equals 1 mN/m, is assumed to correspond to the physical contact between the two opposing NP covered surfaces since no significant long-range interactions are expected. Repeated compression/decompression cycles led to a significant decrease in the onset of the interaction forces from 190 to 132 nm and a change in the shape of the force profile, i.e., from an s-shape to a purely exponential profile. The third compression/decompression cycle was performed 10 h after the completion of the second cycle, suggesting an irreversible deformation of the NPs resulting from the compression/decompression cycles. For small NP grafting densities (1.70 and 0.41 NPs/ μm^2), compression force profiles were purely exponential and showed good reproducibility upon repeated cycling.

Figure 7a shows the NP maximum height measured using AFM after the third force profiles and half the onset of the interaction forces measured by SFA (measured on the third approach) as a function of NP surface coverage. As previously mentioned, the onset of the interaction force is assumed to correspond to twice the height of the NPs under no applied load. Results show an increase in NP height with NP surface coverage. As the center-to-center distance between adjacent NPs at high surface coverage (585 nm for 2.63 NPs/ μm^2 , Figure 5a) is smaller than the diameter of NPs at small surface coverage (700 nm), the NPs are likely to be laterally compressed and therefore deformed for large grafting densities as illustrated in Figure 7b. At small surface coverage, the height of the NPs assessed from the onset of the interaction profiles (37 ± 2 nm) is different from that measured using AFM (45 ± 3 nm). The smaller value measured using SFA might be due to the possible interdigitation between the two opposing NP monolayers of small coverage, i.e., partial insertion of NPs from one monolayer into the free regions of the opposing monolayer (see Figure 7b). For large grafting densities, the NP heights measured with SFA and AFM are similar (59 ± 2 nm and 57 ± 2 nm respectively), suggesting the absence of interdigitation.

The decompression profiles are significantly different from the compression profiles (Figure 6). For all experiments, no adhesion force between the NP monolayers could be measured. For large grafting densities (1.97 and 2.63 NPs/ μm^2), the second and third decompression profiles were very similar, whereas the decompression profiles for small NP surface coverage (1.70 and 0.41 NPs/ μm^2) showed a history effect, i.e., the second and subsequent decompressions are different from the first decompression curve. For 1.70 NPs/ μm^2 , an inflection point is observed for the first decompression, but it is absent on the subsequent profiles (Figure 6). For 0.41 NPs/ μm^2 , an inflection point is observed for the three decompression profiles with a magnitude

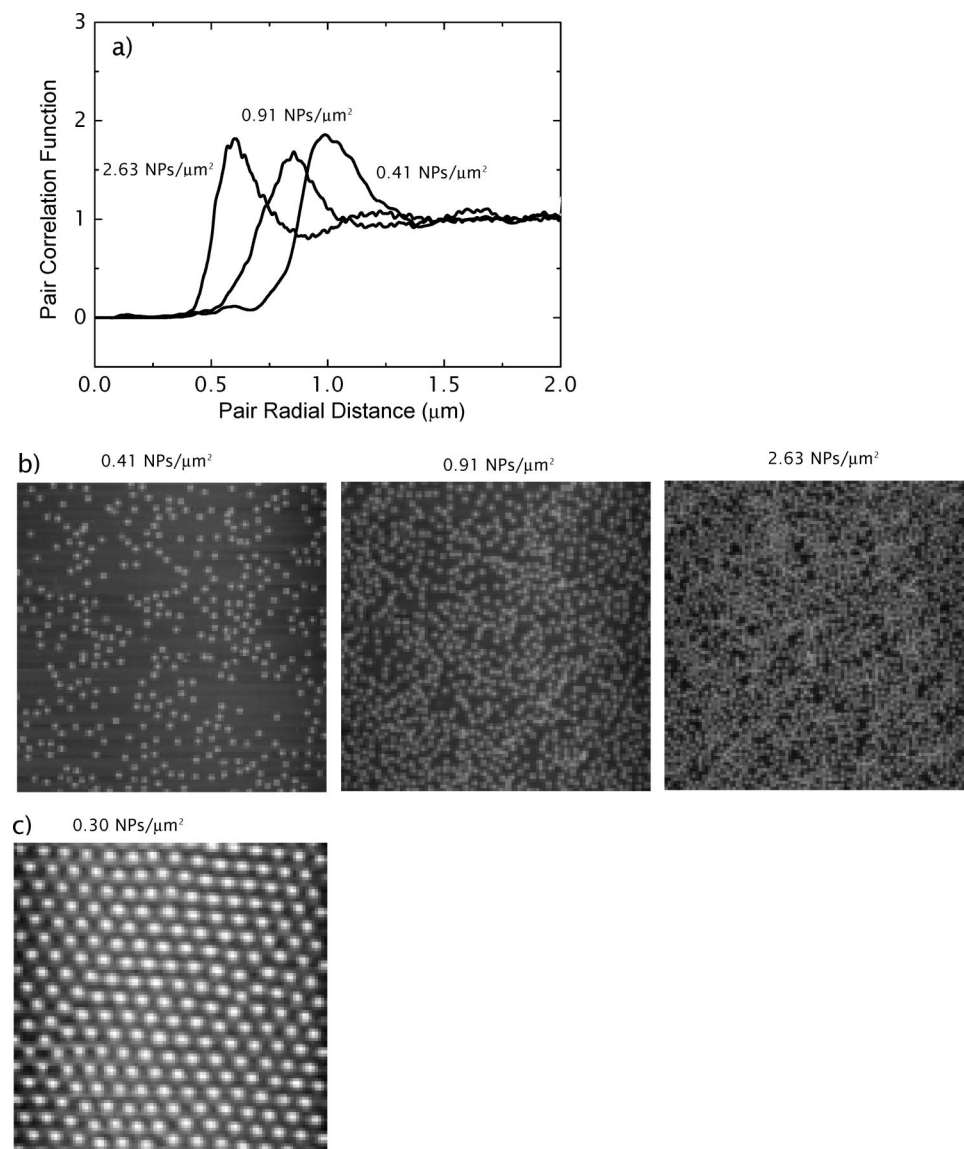


Figure 5. (a) Radial pair correlation function of nanoparticle monolayers grafted on Glu-surfaces for three different grafting densities. (b) AFM images of the monolayers (obtained 24 h after the grafting) in air at 25 °C and 30% RH. (c) AFM image of a nanoparticle monolayer on a bare mica surface (obtained immediately after nanoparticle deposition). Image scale, $30 \times 30 \mu\text{m}$.

TABLE 1: Characteristics of the NP Monolayer

NP surface coverage ^a ($\text{NPs}/\mu\text{m}^2$)	surface rms, ^a R_q (nm)	surface rms slope, ^a R_{dq}	summit curvature ^a (nm)	friction coefficient, ^b μ
0.41	5.5 ± 0.3	0.059 ± 0.001	1102 ± 36	0.031 ± 0.004
1.7	8.5 ± 0.2	0.109 ± 0.001	950 ± 29	0.078 ± 0.008
1.97	10.1 ± 0.1	0.126 ± 0.002	855 ± 21	0.162 ± 0.010
2.63	10.6 ± 0.3	0.139 ± 0.002	828 ± 26	0.324 ± 0.019

^a Values obtained from AFM measurements. ^b Measured using SFA.

varying from 72.8 to 13.8 mN/m from the first to the third decompression.

In order to get more insight on the origin of the hysteresis and history effects, partial force profiles were performed for a NP surface coverage of 0.41 $\text{NPs}/\mu\text{m}^2$. As partial force profile, we mean a compression/decompression cycle carried out over a small range of separation distances, i.e., ranging from the onset of interaction to a distance significantly larger than the hard wall position. A first partial compression/decompression cycle was performed on a new contact position up to a maximum normalized force of 30 mN/m, which is significantly smaller than the magnitude of the first inflection point. The minimum

separation distance of these partial forces profile, i.e., 60 nm, is not sufficient for one NP trapped in between the surfaces to adhere simultaneously on both surfaces, which rule out the possibility of the bridging phenomenon. The partial force profiles were reversible and did not show any inflection point (Figure 8a).

To further investigate the origin of these hysteresis and history effects, we performed complete compression/decompression profiles with inactive remnant carbonyl moieties on the Glu-surfaces. To inhibit the activity of the carbonyl groups, the two NP coated surfaces were separated at a distance of ca. $10 \mu\text{m}$ and immersed in a solution of ethylene glycol at 0.1% w/w for

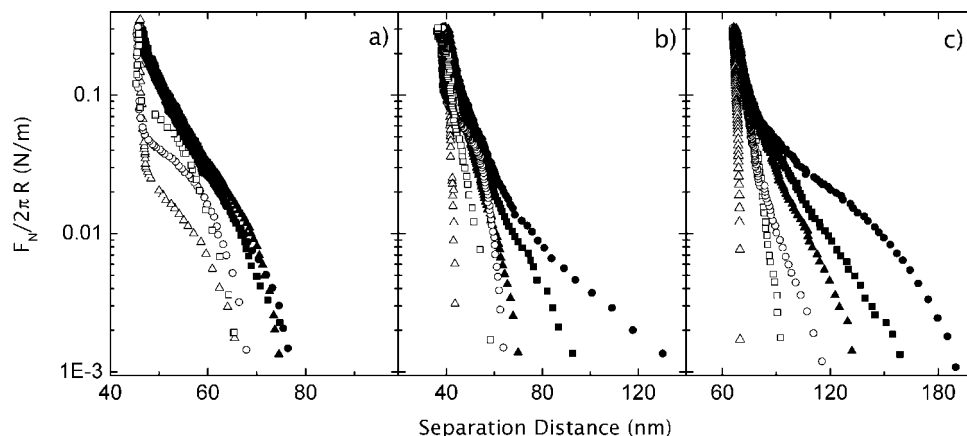


Figure 6. Normalized interaction forces between two opposing nanoparticle monolayers for grafting densities of (a) 0.41 NPs/ μm^2 , (b) 1.70 NPs/ μm^2 , and (c) 2.63 NPs/ μm^2 . Filled and empty symbols are for approach and separation profiles, respectively. \bullet , \circ , first profile; \blacksquare , \square , second profile; \blacktriangle , \triangle , third profile. Data were obtained at 25 °C and 30% RH. The standard deviation of interaction forces is 0.1 mN/m and 1 nm for separation distance.

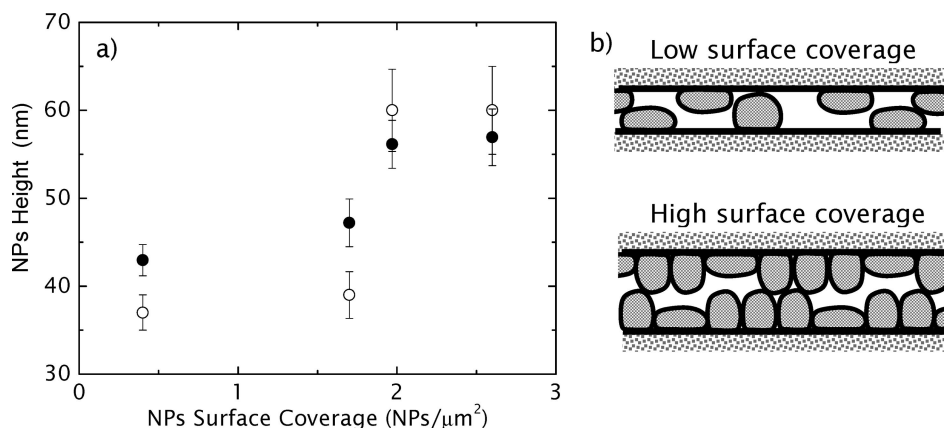


Figure 7. (a) Variation of the nanoparticle maximum height as a function of NP surface coverage using (\bullet) AFM and (\circ) SFA from the onset of interactions on the third approach. The onset of interactions was defined as the separation distance at which the interaction force is 1.0 ± 0.1 mN/m. (b) Schematic view of the evolution of nanoparticle conformation at the onset of the interaction forces with grafting density.

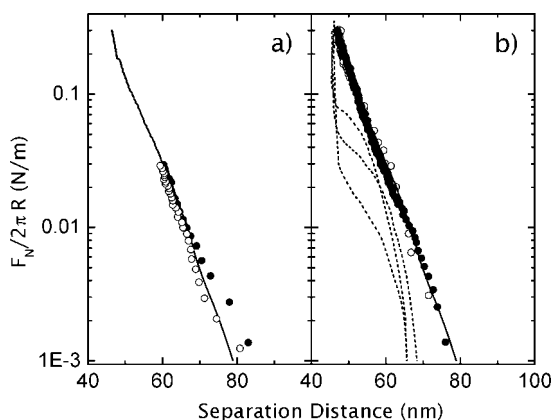


Figure 8. Interaction force profiles for two opposing nanoparticle monolayers for a grafting density of 0.41 NPs/ μm^2 and for a maximum normalized force of (a) 30 mN/m with noninhibited carbonyl moieties and (b) 300 mN/m with inhibition of the remnant carbonyl moieties of the Glu-surface with ethylene glycol (see text for details). Filled and empty symbols are for approach and separation profiles, respectively. The solid and dashed lines correspond to the force profiles reported in Figure 6a.

2 h within the SFA chamber. The ethylene glycol molecules are expected to react with the remnant carbonyl moieties of the Glu-surface, which are located in between the NPs. This would give rise to inactive acetal groups, which do not have affinity with the ethoxy groups of the NPs. Therefore the existence of

any chemical bond between grafted NPs and the opposing surface is precluded. The SFA chamber was rinsed with water and dried for 8 h under pure nitrogen and finally allowed to equilibrate for 8 h in a 30% RH atmosphere. Compression/decompression cycles were then performed to a maximum normalized force of 300 mN/m, which corresponds to the hard wall position measured with noninhibited carbonyl groups (Figure 6). The resulting force profiles, shown in Figure 8b, were completely reversible (no hysteresis), similar to the approach profiles obtained with grafted NPs (Figure 6a) but they did not show any history effect. Therefore, the presence of the inflection point observed in the decompression profiles for small grafting densities (Figure 6) is most presumably due to NPs bridging between the two opposing surfaces, i.e., NPs from one surface can adhere to the available carbonyl functions from the opposing surface when the separation distance is close to the size of one NP. The decrease in the magnitude of the inflection point upon repeated compression/decompression cycles could be due to a progressive damage or degrafting of the silane layer of the Glu-surfaces occurring when bridged NPs are detached from one surface upon decompression.

Mechanical and Adhesive Properties of NP Monolayers.

The variation of the radius of the circular area of contact a between the two opposing NP monolayers as a function of the normal force is illustrated in Figure 9 for NP grafting densities of 0.41 and 2.63 NPs/ μm^2 . For small grafting densities, the a

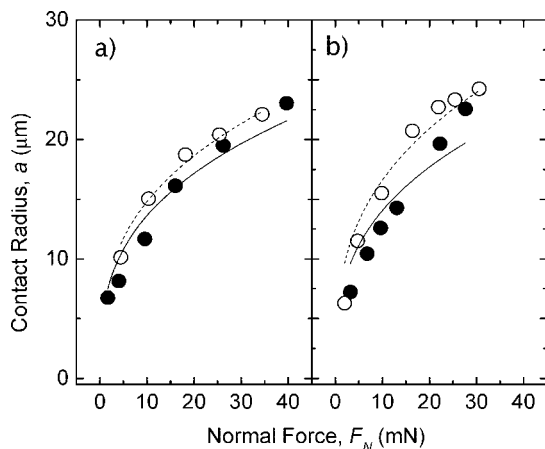


Figure 9. Contact radius between two nanoparticle monolayers grafted on mica surfaces, in the cross-cylinder geometry used in the SFA, as a function of the applied normal force F_N and for grafting densities of (a) 0.41 NPs/ μm^2 and (b) 2.63 NPs/ μm^2 . Filled and open symbols are for approach and separation profiles, respectively. Continuous and dashed lines correspond to the JKR fits (eq 1) for the approach and separation, respectively. The fitted parameters are reported in Table 1. The standard deviation of the contact radius is 2 μm .

versus F_N curves did not exhibit any hysteresis upon compression/decompression cycles. For larger surface coverage (2.63 NPs/ μm^2), hysteresis is observed. We used the well-known Johnson Kendall Roberts (JKR) theory to determine the effective compressive modulus, K (in GPa) and the adhesion force, F_{adh} (in N). In the crossed cylinders geometry, the JKR equation can be expressed as follows:²⁹

$$a^3 = \frac{R}{K} (F_{adh}^{1/2} + (F_{adh} + F_N)^{1/2})^2 \quad (1)$$

where R is the radius of the cylindrical surfaces (0.02 m). The parameters resulting from the fitting are summarized in Table 2. The adhesion force is zero, independent of the NP surface coverage, and the compressive modulus K decreases as the NP surface coverage increases. This compressive modulus K corresponds to an effective value of the whole system, i.e., the silica cylindrical disks, the optical adhesive (ca. 10 μm thick, elastic modulus 1.38 GPa), the mica substrate (2.5 μm thick and elastic modulus 50–100 GPa), and the NP monolayers. As the moduli of the underlying substrate (silica, glue, and mica) are constant for all experiments and as the NP monolayers are expected to be much softer than the other underlying materials,^{30,31} the variation of K with the NP surface coverage can be directly ascribed to the presence of the NPs. Fitting quality assessed by r^2 indicates that the JKR model can represent relatively well the behavior of NPs for small surface coverage compared to large coverage (see Table 2).

Friction Forces between NP Monolayers. Measurements of the friction forces between two opposing NP monolayers in contact under 30% RH conditions at 25 °C were performed at different sliding velocities ranging from 0.23 to 3.06 $\mu\text{m/s}$ and at different normal or compressive forces. Examples of the variation of the friction force with time (friction traces) are illustrated in Figure 10a. The kinetic friction force F_s was determined as the average value obtained at the plateau. Stiction spikes were observed at relatively large compressive forces (>25 mN) and for small sliding velocities (<1 $\mu\text{m/s}$). No stick–slip (SS) transition was observed for all NP surface coverage. Indeed, the relatively large sliding velocities used and the amorphous structure of the NP monolayer are not expected to give rise to stick–slip motions.^{1,32} No significant variation of the friction

force with sliding velocity was observed for all grafting densities and for normal forces lower than 20 mN. For larger normal forces, the friction force F_s increased slightly with an increase in the sliding velocity. The variation of F_s with sliding velocity is illustrated in Figure 10b for an intermediate grafting density of 1.97 NPs/ μm^2 . For all friction measurements, no physical damages or wear tracks were observed under our experimental conditions. Moreover, no friction (static or kinetic) forces could be measured for normal forces smaller than 1 mN/m (onset of interaction). The absence of adhesion between the two opposing NP monolayers (Figure 6) and the presence of bonded water molecules around the NPs could indeed prevent the friction between contacting surfaces under low compressive load as also observed for bare mica surfaces and hydrophilic polymer-coated surfaces in aqueous media.^{33–36} For these nonadhesive surfaces, the experimental data follow Amontons' law $F_s = \mu F_N$ (Figure 11) from which a friction coefficient μ can be extracted. The values of the corresponding friction coefficients are summarized in Table 1.

Discussion

Frictional properties of NP monolayers are expected to depend on mechanical, physical, and adhesive properties of the NPs. The mechanical properties, more specifically the elastoplastic behavior, can be assessed qualitatively via the history effect of the force profiles (Figure 6). For deformation ranging from 0 to 0.4, the compression of dense NP monolayers exhibited a significant history effect (Figure 6c), i.e., elastoplastic behavior, compared monolayers of small surface coverage (Figure 6a) for which the absence of history effect suggests a purely elastic behavior. Moreover, the JKR theory could not represent the experimental data for large grafting densities (>1.97 NPs/ μm^2). In these conditions, contact radius hysteresis upon compression/decompression cycles was significant. Contact radius between rough surfaces is known to deviate strongly from continuum models such as Hertz or JKR theories because these theories intrinsically consider flat contacts between two purely elastic materials.³⁷ More elaborated theoretical studies based on numerical simulations of contact mechanics between nonadhesive elastoplastic materials have shown irreversible deformations manifested by a large hysteresis in compression/decompression cycles.^{38–41}

The surface coverage-dependent mechanical properties can be explained by the change in summit curvature (Table 1). For large NP surface coverage, the NPs are largely deformed because of lateral pressure exerted by the adjacent NPs, giving rise to a decrease in their summit curvature. The summits are expected to undergo plastic deformation when the maximum shear stress at the summit contact exceeds half the yield stress in simple tension. The critical deformation wp at which plastic flow occurs can be written as $wp \approx R_c(Y/E')$, where R_c is the summit curvature, Y is the yield stress in simple tension, and E' is the Young's modulus of the material.⁶ This relationship implies that NPs with smaller summit curvature (i.e., for large grafting densities) are more likely to undergo normal plastic deformation. This plastic deformation might be associated with polymer chain reorganization within the NPs. Indeed, as the cross-linker density in the NPs is not expected to be homogeneous, domains in the NPs where polymeric chains are just entangled can easily flow under compression. Moreover, the energy dissipated by the friction within the polymeric network of the NPs as they are compressed is also a source of mechanical nonrecovery.

To elucidate the role of surface roughness on friction behavior, the friction force as a function of normal force was

TABLE 2: Fitted Parameters from the JKR Theory (Eq 1) for Different NP Grafting Densities

NP surface coverage (NPs/ μm^2)	K^a (GPa)	from compression profiles		from separation profiles	
		F_{adh}^b (N)	r^2^c	F_{adh} (N)	r^2
0.41	79.0 ± 10.1	0	0.95	0	0.97
1.7	77.1 ± 3.1	0	0.96	0	0.95
1.97	74.2 ± 6.4	0	0.89	0	0.87
2.63	71.1 ± 19.8	0	0.88	0	0.82

^a Compression modulus. ^b Adhesion force. ^c Normalized root-mean-square error.

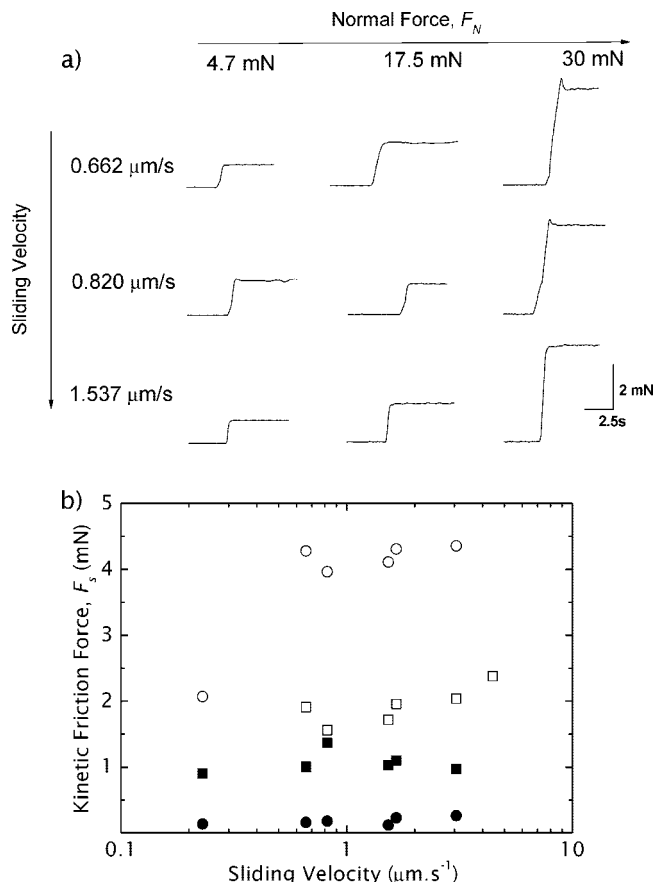


Figure 10. (a) Friction traces obtained between two opposing nanoparticle monolayers in contact under different normal forces and sliding speeds for a NP grafting density of 1.97 NPs/ μm^2 . (b) Reported kinetic friction force F_s obtained from the plateau values of the friction traces as a function of sliding velocity for different normal forces: \circ , 30.0 mN; \square , 17.5 mN; \blacksquare , 12.1 mN; \bullet , 4.7 mN. The standard deviation of the friction force is 0.05 mN.

determined for different grafting densities and therefore for different surface roughnesses. The linear dependence of kinetic friction F_s on normal force F_N was observed for all grafting densities, i.e., $F_s = \mu F_N$. This linearity was expected since there was no adhesion measured between the NP monolayers and because the surfaces are rough, implying an increase in the real contact area with an increase in normal force. For rms ranging from ca. 5 to 8 nm, μ ranges from ca. 0.03 to 0.08, which is much smaller than the values reported for polymer rough surfaces ($\mu = 0.5\text{--}1.3$ for a rms ranging from 2.5 to 7.1 nm)⁸ but close to reported values for hydrogel.⁴²

Elastoplastic behavior has previously been associated with low friction forces, compared to purely elastic material, in experimental^{43,44} and theoretical^{44,45} studies, even though the impact of the elastoplastic behavior on the friction coefficient is expected to be rather small compared to the effect of surface topography.^{43–45} Our experimental data are not in agreement

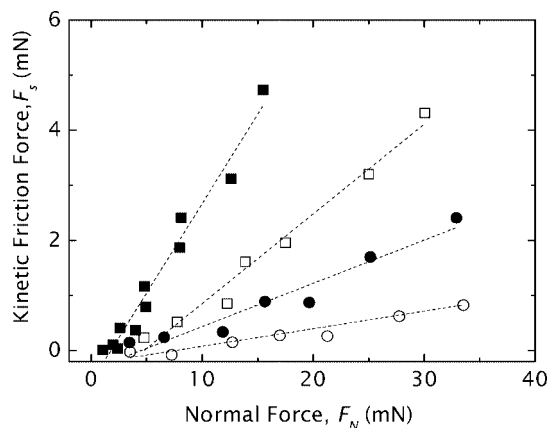


Figure 11. Kinetic friction force F_s between two opposing nanoparticle monolayers as a function of the normal force F_N in air at 25 °C and 30% RH for a sliding velocity of 1.66 $\mu\text{m/s}$ and grafting densities of \blacktriangle , 0.41 NPs/ μm^2 ; \bullet , 1.70 NPs/ μm^2 ; \square , 1.97 NPs/ μm^2 ; and \blacksquare , 2.63 NPs/ μm^2 . Dashed lines are linear fits whose slope corresponds to the friction coefficient μ . The standard deviation of the friction force is 0.05 mN. The friction coefficients are reported in Table 1.

with these studies as they indicate a significant increase in the friction forces with increasing plasticity. However, our results suggest a correlation between the friction coefficient μ and surface topography. A quasi exponential increase in μ with increasing R_q and R_{dq} is observed (Table 2) as previously reported experimentally^{46–48} and theoretically^{49,50} for rough surfaces. A ratchet mechanism, developed by Tabor,⁵¹ has been proposed to explain this behavior. This mechanism considers that asperity contacts are tangential to the supporting substrate. This mechanism is dissipative, i.e., the energy expended in ascending the asperities is large compared to the one expended in descending motion because of the presence of impact deformation and phonon generation.⁵² Theoretical simulations based on GW formalism have shown that the increase in the friction coefficient with increasing surface roughness of elastoplastic materials could be entirely explained by this ratchet mechanism.⁵⁰ Our experimental results, i.e., surface roughness-dependent friction coefficient, are also consistent with this analysis and suggest that a similar mechanism occurs between two opposing sliding NP monolayers.

Conclusions

The normal and lateral interaction forces between two monolayers of polymer nanoparticles grafted on functionalized mica substrates in humid atmosphere were measured. The relationship among the NP surface coverage, surface roughness, NP mechanical properties, and the resulting frictional properties was investigated. An increase in NP surface coverage was inherently associated with an increase in surface roughness, with a plastic deformation of the NPs upon normal compression and with an increase in friction. Friction measurements revealed a quasi exponential increase in the friction coefficient μ with

surface roughness as predicted by a frictional ratchet mechanism previously proposed for rough surfaces.

Acknowledgment. This work was supported by the Natural Sciences and Engineering Research Council (NSERC). We thank Professor R. E. Prud'homme for providing access to his AFM facilities and E. Weeks for fruitful discussions.

References and Notes

- (1) Maeda, N.; Chen, N. H.; Tirrell, M.; Israelachvili, J. N. *Science* **2002**, 297, 379.
- (2) Cumings, J.; Zettl, A. *Science* **2000**, 289, 602.
- (3) Liley, M.; Gourdon, D.; Stamou, D.; Meseth, U.; Fischer, T. M.; Lautz, C.; Stahlberg, H.; Vogel, H.; Burnham, N. A.; Duschl, C. *Science* **1998**, 280, 273.
- (4) Urbakh, M.; Klafter, J.; Gourdon, D.; Israelachvili, J. *Nature* **2004**, 430, 525.
- (5) Bhushan, B. *Introduction to Tribology*; John Wiley: New York, 2002.
- (6) Greenwood, J.; Williams, J. *Proc. R. Soc. London, A* **1966**, 295, 300.
- (7) Bhushan, B. *Handbook of Micro/Nano Tribology*, 2nd ed.; CRC Press: New York, 1999.
- (8) Zappone, B.; Rosenberg, K. J.; Israelachvili, J. *Tribol. Lett.* **2007**, 26, 191.
- (9) Colonne, M.; Chen, Y.; Wu, K.; Freiberg, S.; Giasson, S.; Zhu, X. X. *Bioconjugate Chem.* **2007**, 18, 999.
- (10) Hong, H. G.; Jiang, M.; Sligar, S. G.; Bohn, P. W. *Langmuir* **1994**, 10, 153.
- (11) Jonsson, U.; Olofsson, G.; Malmqvist, M.; Ronnberg, I. *Thin Solid Films* **1985**, 124, 117.
- (12) Banquy, X.; Rabanel, J. M.; Hildgen, P.; Giasson, S. *Aust. J. Chem.* **2007**, 60, 638.
- (13) Liberelle, B.; Giasson, S. *Langmuir* **2007**, 23, 9263.
- (14) Jirku, V.; Turkova, J. *Methods Enzymol.* **1987**, 135, 341.
- (15) Mansson, M. O.; Mosbach, K. *Methods Enzymol.* **1987**, 136, 3.
- (16) Prevo, B. G.; Velev, O. D. *Langmuir* **2004**, 20, 2099.
- (17) Israelachvili, J. N. *J. Colloids Interface Sci.* **1973**, 44, 259.
- (18) Israelachvili, J. N.; Adams, G. E. *J. Chem. Soc., Faraday Trans.* **1978**, 174, 975.
- (19) Israelachvili, J. N.; McGuiggan, P. M. *J. Mater. Res.* **1990**, 5, 2223.
- (20) Israelachvili, J. N.; McGuiggan, P. M.; Homola, A. M. *Science* **1988**, 240, 189.
- (21) Zhang, F. X.; Srinivasan, M. P. *Langmuir* **2004**, 20, 2309.
- (22) Bierbaum, K.; Kinzler, M.; Woll, C.; Grunze, M.; Hahner, G.; Heid, S.; Effenberger, F. *Langmuir* **1995**, 11, 512.
- (23) Okusa, H.; Kurihara, K.; Kunitake, T. *Langmuir* **1994**, 10, 3577.
- (24) Herder, P.; Vagberg, L.; Stenius, P. *Colloids Surf.* **1988**, 34, 117.
- (25) Prevo, B. G.; Kuncicky, D. M.; Velev, O. D. *Colloids Surf., A* **2007**, 311, 2.
- (26) Prevo, B. G.; Hwang, Y.; Velev, O. D. *Chem. Mater.* **2005**, 17, 3642.
- (27) Prevo, B. G.; Hon, E. W.; Velev, O. D. *J. Mater. Chem.* **2007**, 17, 791.
- (28) Degennes, P. G. *Macromolecules* **1980**, 13, 1069.
- (29) Johnson, K. L.; Kendall, K.; Roberts, A. D. *Proc. R. Soc. London, A* **1971**, 324, 301.
- (30) Tagit, O.; Tomczak, N.; Vancso, G. J. *Small* **2008**, 4, 119.
- (31) Wiedemair, J.; Serpe, M. J.; Kim, J.; Masson, J. F.; Lyon, L. A.; Mizaikoff, B.; Kranz, C. *Langmuir* **2007**, 23, 130.
- (32) Luan, B. Q.; Robbins, M. O. *Phys. Rev. E* **2006**, 74.
- (33) Chai, L.; Klein, J. *Macromolecules* **2008**, 41, 1831.
- (34) Gourdon, D.; Lin, Q.; Oroudjev, E.; Hansma, H.; Golan, Y.; Arad, S.; Israelachvili, J. *Langmuir* **2008**, 24, 1534.
- (35) Raviv, U.; Giasson, S.; Kampf, N.; Gohy, J. F.; Jerome, R.; Klein, J. *Nature* **2003**, 425, 163.
- (36) Klein, J.; Raviv, U.; Perkin, S.; Kampf, N.; Chai, L.; Giasson, S. *J. Phys.: Condens. Matter* **2004**, 16, S5437.
- (37) Luan, B. Q.; Robbins, M. O. *Nature* **2005**, 435, 929.
- (38) Chang, W. R.; Etsion, I.; Bogy, D. B. *J. Tribol.* **1987**, 109, 257.
- (39) Chang, W. R. *Wear* **1997**, 212, 229.
- (40) Zhao, Y. W.; Maietta, D. M.; Chang, L. *J. Tribol.* **2000**, 122, 86.
- (41) Pei, L.; Hyun, S.; Molinari, J. F.; Robbins, M. O. *J. Mech. Phys. Solids* **2005**, 53, 2385.
- (42) Gong, J. P. *Soft Matter* **2006**, 2, 544.
- (43) Nelias, D.; Antaluca, E.; Boucly, V.; Cretu, S. *J. Tribol.* **2007**, 129, 761.
- (44) Lafaye, S.; Gauthier, C.; Schirrer, R. *J. Mater. Sci.* **2006**, 41, 6441.
- (45) Bellemare, S.; Dao, M.; Suresh, S. *Int. J. Solids Struct.* **2007**, 44, 1970.
- (46) Chang, W. R. *Safety Sci.* **1998**, 29, 89.
- (47) Hayward, I. P.; Singer, I. L.; Seitzman, L. E. *Wear* **1992**, 157, 215.
- (48) Wong, H. C.; Umehara, N.; Kato, K. *Wear* **1998**, 218, 237.
- (49) Daikhin, L.; Urbakh, M. *Phys. Rev. E: Stat. Phys., Plasmas, Fluids, Relat. Interdiscip. Top.* **1994**, 49, 1424.
- (50) Ford, I. J. *J. Phys. D: Appl. Phys.* **1993**, 26, 2219.
- (51) Tabor, D. *The Properties of Diamond*; Academic Press: London, 1979.
- (52) Samuels, B.; Wilks, J. *J. Mater. Sci.* **1988**, 23, 2846.

JP803605D